

See discussions, stats, and author profiles for this publication at: <https://www.researchgate.net/publication/266204810>

Cu₂ZnSn(S, Se)₄ thin film absorbers based on ZnS, SnS and Cu₃SnS₄ nanoparticle inks: Enhanced solar cells performance by using a two-step annealing process

ARTICLE *in* SOLAR ENERGY MATERIALS AND SOLAR CELLS · JANUARY 2015

Impact Factor: 5.34 · DOI: 10.1016/j.solmat.2014.08.024

CITATIONS

8

READS

308

4 AUTHORS, INCLUDING:



Xianzhong Lin

Helmholtz-Zentrum Berlin

22 PUBLICATIONS 137 CITATIONS

SEE PROFILE



Ahmed Ennaoui

Qatar Foundation

198 PUBLICATIONS 3,262 CITATIONS

SEE PROFILE

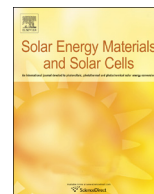


Martha Ch. Lux-Steiner

Helmholtz-Zentrum Berlin

591 PUBLICATIONS 7,839 CITATIONS

SEE PROFILE



Cu₂ZnSn(S, Se)₄ thin film absorbers based on ZnS, SnS and Cu₃SnS₄ nanoparticle inks: Enhanced solar cells performance by using a two-step annealing process

Xianzhong Lin*, Jaison Kavalakkatt, Ahmed Ennaoui, Martha Ch. Lux-Steiner

Helmholtz-Zentrum Berlin für Materialien und Energie, Hahn-Meitner-Platz 1, D-14109 Berlin, Germany

ARTICLE INFO

Article history:

Received 9 July 2014

Received in revised form

12 August 2014

Accepted 22 August 2014

Keywords:

Solution process

CZTS

Solar cells

ABSTRACT

In this paper, we present the fabrication of Cu₂ZnSn(S, Se)₄ (CZTSSe) thin film absorbers by a four-step solution process based on ZnS, SnS and Cu₃SnS₄ nanoparticle precursors and their application in thin film solar cells. The influence of ligand-exchange process on the morphologies of the resulting CZTSSe thin films was studied. Ligand exchange with each sequential spun coat layers leads to cracking films which can be avoided by combining ligand-exchanged and non-ligand-exchanged processes. Moreover, a two-step annealing process yields the most homogeneous films. CZTSSe thin films consisting a large grain and fine nanoparticle grain layered structure was formed. The formation of layered structure for the absorbers was found to be due to the existence of high content of carbon left near the back contact and the out diffusion of Cu and Zn from the bottom layer to the surface layer. As a result, solar cell conversion efficiency was improved from 1.2% to 3.0% upon adoption a two-step annealing process. Temperature dependent *I*–*V* characteristic analysis reveals the dominant loss mechanism of the solar cells is the strong CZTSSe and CdS buffer interface recombination.

© 2014 Elsevier B.V. All rights reserved.

1. Introduction

As a p-type semiconductor material, Cu₂ZnSn(S, Se)₄ (CZTSSe) has emerged as a promising candidate for solar energy conversion. The optical band gap of this material can be tuned between 1.0 eV and 1.5 eV by changing [S]/([S]+[Se]) ratio, which matches very well with the solar spectrum. Meanwhile, the absorption coefficient of CZTSSe is over 10⁴ cm^{−1} in the visible region, which means that 1–2 μm thick CZTSSe is enough for absorbing most of the light. Although Cu(In,Ga)Se₂ (CIGS)-based solar cells with an efficiency of 20.9% [1] have been achieved, the use of In as a constituent has been an issue for the high raw material cost. CZTSSe showing similar optoelectronic properties with CIGS but containing much more earth-abundant constituents compared with CIGS have exhibited great potential in thin film solar cells application as alternative absorber layers. Various approaches have been applied to deposit CZTSSe thin films, including vacuum-based techniques [2–5] (e.g. evaporation) and solution-based techniques (hydrazine-based [6–9], nanoparticle-based [10,11], molecular ink based [12–17] and electrodeposition [18–21]). Among these methods, the hydrazine-based solution process yielded the best solar cells with an efficiency of

12.6% as reported by Wang et al. [7]. CZTSSe solar cells with efficiencies over 8% have also been fabricated by nanoparticle based method and electrodeposition [14,19,20]. On the other hand, 9.15% efficient CZTSe solar cells have been reported by Repins et al. [3] using the co-evaporation technique. All these results point to the promising of CZTSSe as thin film absorbers for solar energy conversion.

As it is reported, the CZTSSe-based solar cell performances are strongly related to the chemical composition of the absorber layers, particularly the ratios of Cu/(Zn+Sn) and Zn/Sn. Previously, we have reported that CZTS thin film absorbers can be fabricated from ZnS and Cu₃SnS₄ (CTS) nanoparticle ink precursors by a spin coating process [22], where both CTS and evaporated Sn was used as Sn source for CZTS. To avoid using the vacuum process for the Sn source and to get a better control over the chemical composition of the resulting absorber layers, SnS nanoparticles are used as the third precursor. Accordingly, the chemical composition of resulting thin film absorbers can be tuned by adjusting the ratios of the ZnS, SnS and Cu₃SnS₄ nanoparticle precursors.

One of the important issues for using nanoparticles which is generally stabilized by a long chain organic ligand is that it is difficult to completely remove the ligand after deposition of thin films. The existence of the long chain ligand in the thin films may hinder the charge transfer in the thin films. One way to solve this problem is to perform ligand exchange with a shorter chain

* Corresponding author.

E-mail address: lin.xianzhong@helmholtz-berlin.de (X. Lin).

ligand or inorganic ligand. For example, Zhang et al. [23] reported to completely remove the organic ligand in PbS nanocrystal films by dipping PbS nanocrystal thin films in a $(\text{NH}_4)_2\text{S}$ methanol solution. However, cracks were formed in the thin films after ligand exchange due to the reducing of the interparticle distance. These cracks are harmful for the solar cell performance by creating shunting tunnels. Therefore, in this paper we report on the formation of CZTSSe thin film absorbers from a solution process based on ZnS, SnS and Cu_3SnS_4 nanoparticle ink precursors. Particularly, the influence of the combination of the ligand-exchanged process and non-ligand-exchanged process on the morphologies and solar cells performance of resulting CZTSSe thin films were investigated.

2. Materials and methods

2.1. Synthesis of ZnS, SnS and Cu_3SnS_4 nanoparticle precursors

All the nanoparticles including ZnS, SnS and Cu_3SnS_4 were synthesized by a heating-up process [24]. Depending on the samples, oleylamine (OLA) or both OLA and 1-dodecanethiol was used as solvent and capping agents. The precursors, organic solvent and capping agents were mixed in a three-neck round-

bottom reaction flask in air. The flask was removed to the glove box which was filled with nitrogen to avoid the oxidation of the nanoparticles. The reaction mixtures were heated to 130 °C with an increasing rate of 10 °C/min and held at this temperature for 30 min. After that, the reaction mixtures were further heated to desired temperature depending on the sample prepared. The mixtures were kept at this temperature for certain time to allow the growth of the nanoparticles.

The reaction temperature and time can be found in Table S1. After cooling to room temperature, the nanoparticles were precipitated by addition excessive ethanol (for SnS and Cu_3SnS_4 nanoparticles) or acetone (for ZnS nanoparticles) to the flask and isolated by centrifugation at 6000 rpm for 10 min. The supernatant was discarded while the precipitate was dispersed in 4 ml toluene. The precipitation and isolation procedures were repeated one (for SnS and Cu_3SnS_4 nanoparticles) or two more times (for ZnS nanoparticles) to remove the excess organic surfactant. Finally, the nanoparticles were dispersed in toluene or 1-hexanthiol.

2.2. Deposition of $\text{Cu}_2\text{ZnSn(S, Se)}_4$ thin film absorbers

CZTSSe thin films were deposited by a four-step process, as shown in Fig. 1. Firstly, the inks were formed by mixing the ZnS, SnS and CTS nanoparticles with certain ratio in 1-hexanthiol, and then the Cu–Zn–Sn–S precursor thin films were deposited by spin coating. To remove the residual solvent as well as the organic surfactant surrounding the nanoparticles, heat treatments at 170 °C and 350 °C for 2 min were performed, respectively. Ligand-exchange with 0.04 M $(\text{NH}_4)_2\text{S}$ methanol solution was carried out after the sample cooling down to room temperature from the 170 °C heat treatment step. To reach micrometer thick thin films, steps two and three were repeated. The Cu–Zn–Sn–S precursors' thin films were further annealed at 580 °C under S/Se-containing atmosphere for 25 min to form the kesterite CZTSSe thin film absorbers. It should be noted that some of the spin coated layers were not subjected to the ligand-exchanged procedure; detailed information can be found in Table 1.

2.3. Fabrication of solar cells

Prior to the chemical bath deposition of CdS buffer layers, CZTSSe thin film absorbers were first etched by KCN for 5 min. The solar cells were completed by sputtering of ZnO and aluminum doped ZnO window layers and evaporation of Ni:Al grids. Solar cells were separated into 0.5 cm² by mechanical scribing.

2.4. Characterization

X-ray diffraction (XRD) was used to characterize the structural properties of the nanoparticles and the CZTSSe thin films. The nanoparticle samples for the XRD were prepared by drop-casting of the nanoparticle inks onto the glass substrates and dry in air. The measurements were operated on a Bruker D8-Advance X-ray

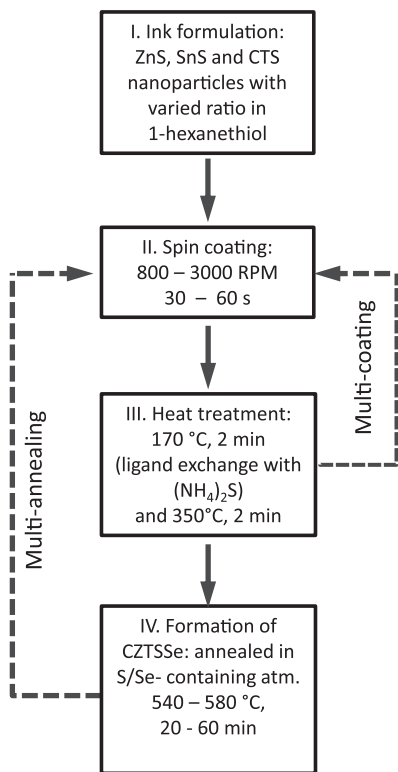


Fig. 1. Schematic diagram showing the preparation process of CZTSSe thin films.

Table 1
Detail preparation parameters of CZTSSe samples with different deposition procedures.

| Samples | Precursors | No. of layers | Annealing conditions | | | Ligand-exchange with 0.04 M $(\text{NH}_4)_2\text{S}$ Me–OH solution for around 30 s |
|---------|----------------------------------|---------------|----------------------|--------|------------|--|
| | | | Time (min) | T (°C) | Atmosphere | |
| A | 0.67 mmol CTS, 1.37 mmol ZnS and | 4 | 25 | 580 | Ar–Se | All four layers |
| B | 0.45 mmol SnS | 5 | | | | First four spin coated layers |
| C | | 4 | | | | First spin coated layer |
| D | 0.67 mmol CTS, 1.45 mmol ZnS and | 3 | 5 | | | Only for the first two spin coated layers |
| | 0.65 mmol SnS | 2 | 25 | | | Only for the last spin coated layer |

diffractometer with Cu K α 1 radiation using a step size of 0.02° and step time of 5 s. Transmission electron microscopy (TEM) was used to analyze the morphology of the nanoparticle samples. TEM samples were prepared by dropping diluted nanoparticles solution onto a carbon film coated gold or copper grids and a Philips CM12 transmission electron microscopy with 120 kV acceleration voltage was used to acquire TEM images of the nanoparticles. Energy dispersive X-ray (EDX) spectroscopy measurement was also performed to the chemical composition of the samples during the TEM measurement. For the Raman measurement a Ti:Sapphire-ring-laser was used as an excitation. The wavelength of the laser is fully tunable from 690 nm to 1050 nm. To avoid laser heating

the beam power was kept below 3.5 mW. Raman spectra were recorded with a Horiba T64000 triple monochromator system in back scattering configuration with a microscope and a motorized XY stage. The micro-Raman spectroscopy with a 100 \times objective was performed at room temperature for a wavelength of 747 nm. The morphologies and chemical composition of the CZTSSe absorbers are analyzed in a LEO 1530 GEMINI scanning electron microscope (SEM) of Zeiss. The SEM images were recorded at an acceleration voltage of 10 kV. The chemical composition was extracted from energy dispersive X-ray (EDX) measurement in the SEM. The EDX measurements were performed at an acceleration voltage of 10 kV by a Thermo Noran X-ray silicon drift detector (acquisition and evaluation software Noran System Seven). The electrical characterization has been performed using an in-house class A sun simulator under standard test conditions (AM 1.5G, 100 mW/cm² and 23 °C). Temperature dependent J – V measurements on the best cells were carried out inside a cryostat which has a transparent window allowing the light pass through. The samples were mounted on a hollowed steel stage which can be flooded with liquid nitrogen to cool down the sample. The temperature was detected by a thermocouple and balanced by an electrical heater. During the measurement, the cryostat is maintained at a pressure of about 10^{−6} mbar by using a turbo pump. The measuring temperature was in the range of 150–300 K in step of 10 K. The sample is illuminated by a single halogen lamp and there is a shutter to switch from dark to illuminated conditions. It should be noted that a single halogen lamp used leads to differences in the spectral content compared to the measurements under standard sun simulator. The mismatch was partly compensated by adjusting the short circuit current to be the same as measured under standard sun simulator, which was fulfilled by adjusting the distance between the lamp and the solar cell

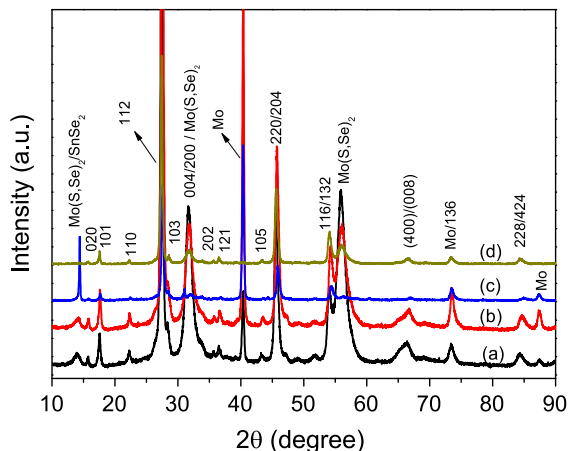


Fig. 2. XRD pattern of different CZTSSe samples: (a) samples A, (b) sample B, (c) sample C, and (d) sample D.

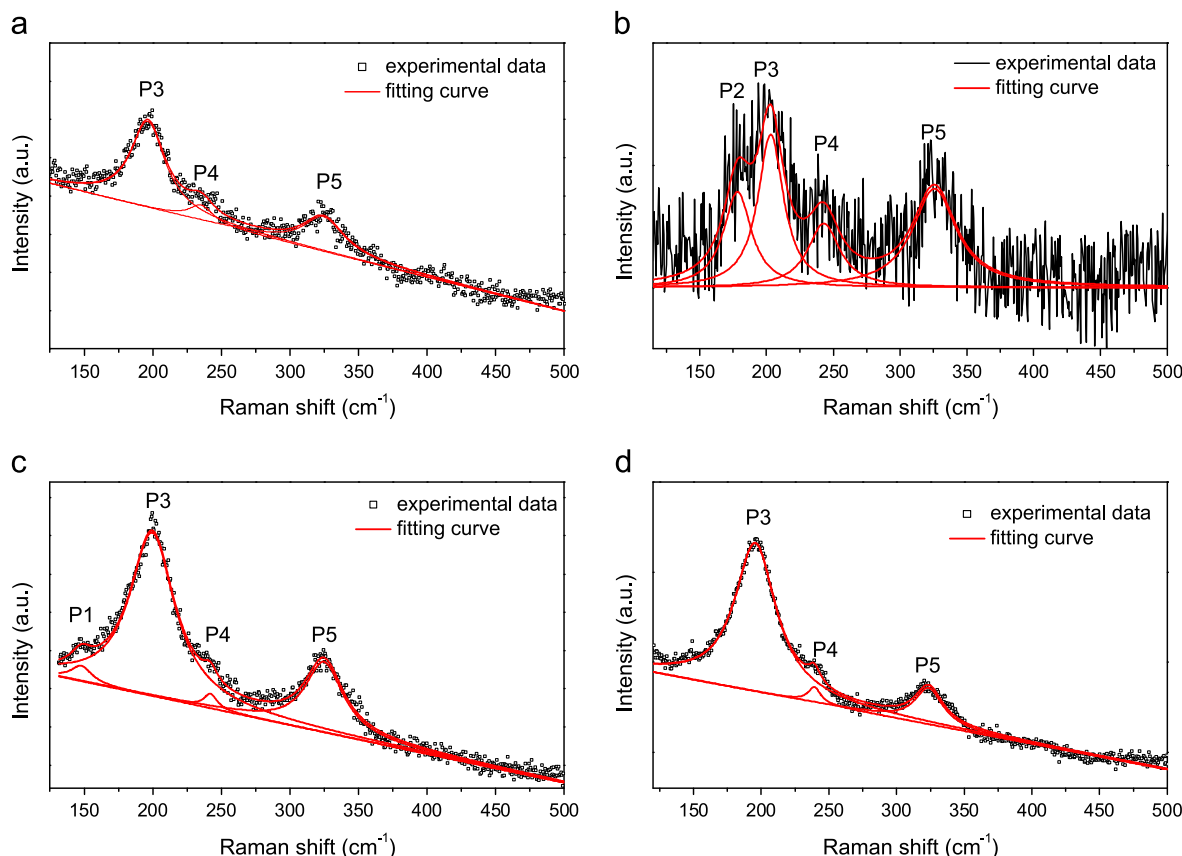


Fig. 3. Raman spectra of CZTSSe samples from different processing conditions: (a) samples A; (b) sample B, (c) sample C, and (d) sample D. Fitting curves using software Peak-O-Mat were also shown.

measured. This ensures that the current flowing across the device is the same as that obtained under one sun simulator. Quantum efficiency analysis has been performed using an illumination system including two sources (halogen and xenon lamps) and a Bentham TM300 monochromator (Bentham Instruments, Berkshire, UK). Reference measurements were performed on calibrated Si and Ge detectors.

3. Results and discussions

Prior to the deposition of the CZTSSe thin films, the morphologies and structure of as-synthesized ZnS, SnS and CTS nanoparticles were characterized by transmission electron microscope and X-ray diffraction. The results of ZnS and SnS nanoparticles can be found in [Supporting information](#). Detail characterization of CTS can be found in our previous paper [\[24\]](#).

[Fig. 2](#) shows the XRD patterns of the samples prepared under different conditions. Diffraction peaks corresponding to tetragonal structure CZTSSe can be found in all four samples. These XRD patterns were shifted to lower angles compared to the pure sulfide CZTS, which is due to the expansion of the lattice constants resulting from the replacement of S with Se in CZTS. Besides to those peaks assigned to CZTSSe, peaks corresponding to Mo

substrates were also observed. It should be noted that secondary phase SnSe₂ was also detected in sample C as evidenced by the peak located at $2\theta = 14.4^\circ$. In addition, Mo(S,Se)₂ phases were also observed in all four samples. The formation of CZTSSe can be explained by the following chemical reaction:



Since the main peaks of secondary phases such as ZnS and CTS is overlapping with CZTS peaks, it is important to use another method to identify the phase purity. Raman spectroscopy have been demonstrated to be a powerful tool for determining the phase purity of kesterite samples. Therefore, Raman spectroscopy measurements were carried out on all four samples to further confirm the formation of CZTSSe phases. The Raman spectra including the measured spectra and fitting curves fitted by using the software Peak-O-Mat with a Lorentzian function are shown in [Fig. 3](#). The peak position of each sample is listed in [Table 2](#). All the spectra show a bimodal behavior where both the Raman A modes of CZTSe and CZTS (peaks of P3 and P5) were detected. This behavior is in good agreement with the literature reports for the CZTSSe compound containing both sulfur and selenium [\[25,26\]](#). Except those peaks corresponding to CZTSSe, peaks corresponding secondary phases were not detected.

[Fig. 4\(a\)](#) shows the surface SEM image of the A sample prepared using a sequential deposition of four layers with each layer ligand-exchange with (NH₄)₂S. Lots of cracks in around 1 μ m can be observed in this resulting CZTSSe thin film, which is due to reduction of interparticle spacing resulting from the replacement of the long chain organic ligand with (NH₄)₂S. Actually, Zhang et al. [\[23\]](#) have also observed cracks in the PbS thin films after replacing the long chain oleate acid ligand with (NH₄)₂S. This is not good for solar cell applications because cracks may lead to shunts in the solar

Table 2
Raman peaks of samples A, B, C, and D.

| Samples | P1 (cm ⁻¹) | P2 (cm ⁻¹) | P3 (cm ⁻¹) | P4 (cm ⁻¹) | P5 (cm ⁻¹) |
|---------|------------------------|------------------------|------------------------|------------------------|------------------------|
| A | – | – | 196 | 235 | 325 |
| B | – | 178 | 203 | 243 | 326 |
| C | 148 | – | 200 | 242 | 325 |
| D | – | – | 196 | 239 | 324 |

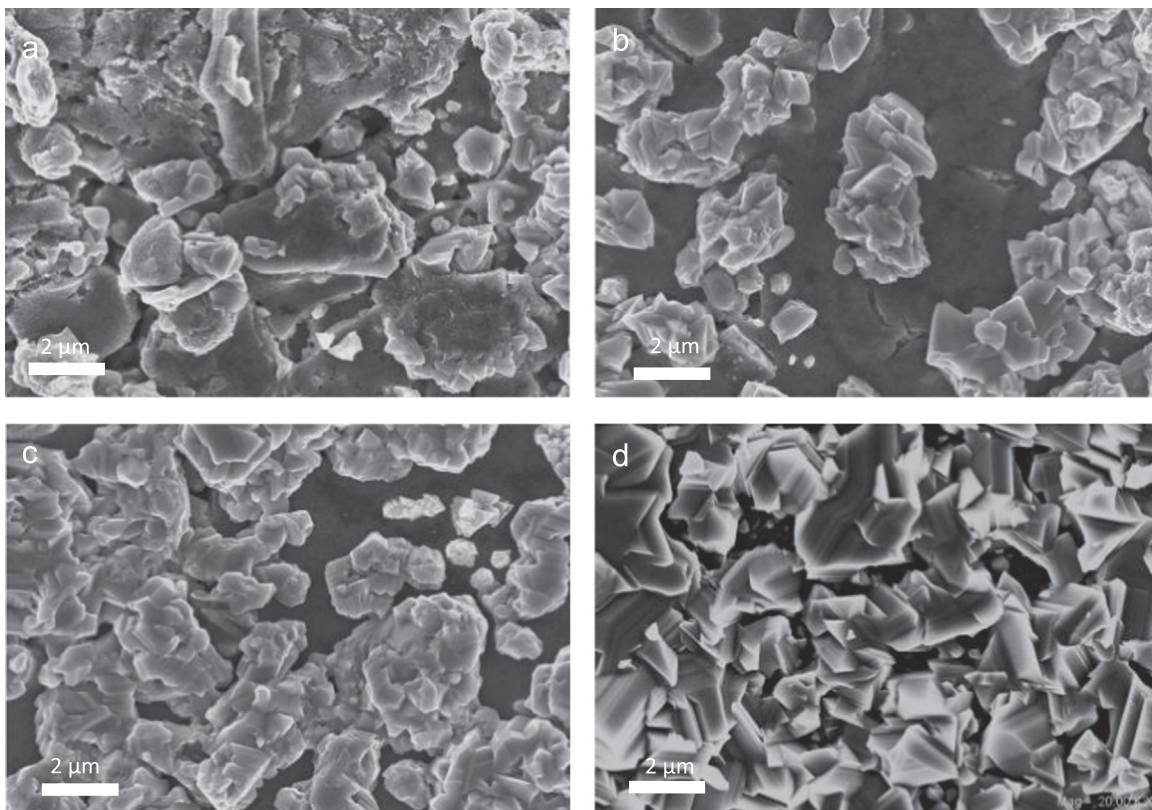


Fig. 4. Surface SEM images of CZTSSe samples prepared with different ligand exchange processes: (a) samples A: ligand-exchange with all four-layers, (b) sample B: four ligand-exchanged layers covered with one without ligand-exchanged layer, (c) sample C: one ligand-exchanged layer cover with three without ligand-exchanged layers, and (d) sample D: two-step annealing.

cells. To minimize the cracks, we modified the deposition processes by combining ligand-exchanged and non-ligand-exchanged processes. Fig. 4(b) shows surface morphology SEM image of sample B deposited by covering four ligand-exchanged layers with one non-ligand exchanged layer. Cracks with size around 150 nm can still be observed on the surface of the samples, although their size is much smaller than that observed in sample A. Additionally, large grains can be detected on the surface; however, the coverage of the grains on the surface is inhomogeneous. Further optimizing the deposition procedures by covering the ligand-exchanged layers with three nonligand-exchanged layers, better coverage of the grains on the surface can be achieved, as shown in Fig. 4(c). By using a two-step annealing process, more homogeneous films can be obtained, see Fig. 4(d).

Fig. 5 shows the cross sectional SEM images of samples C and D. The CZTSSe absorbers have a thickness of 2.0–2.5 μm and 4.4–4.9 μm for samples C and D, respectively. The most reported thickness for CZTSSe absorbers is between 1.0 and 2.5 μm [27–32]. The thickness of sample C is comparable with the most reported values while the thickness of sample D is near twice of the value reported by Mitzi et al. [30–32]. Sample C (Fig. 5(a)) shows a double-layered structure with a large grain layer on top and a fine grain layer near the Mo substrate. Sample D (Fig. 5(b)) shows a more complicated four-layered-structure with a large grain layer on top and another large grain layer located in between two fine grain layers. Interestingly, the coverage of both the large grain layers over the fine grain layer is quite conformal. The formation of this four-layered-structure is because the grain island resulting from the first annealing can be coverage with new coming precursors from the second deposition and further grow together with the precursor during the second annealing. Since the thickness of the second deposition is rather thick, a top large grain layer was also formed. However, we have observed that a double-layered structure can also be realized using this two-step annealing process by reducing the thickness of the second coated precursor layer (see Fig. 6).

To check the homogeneity of the elemental distribution through the cross section of the films, we performed EDX line scanning across the cross section of samples C and D. Fig. 5 (c) shows the EDX line scanning through the cross section for sample C. Four regions are marked over the EDX line scanning: regions of I, II, III and IV correspond the surface of the sample, large grain layer, fine grain layer and Mo substrate. The surface (region I) and the large grain layer (region II) shows a homogeneous distribution of all the elements. However, unlike regions I and II, the fine grain layer shows inhomogeneous distribution for all the elements. The content of C and O increased dramatically from less than 10 at% and 5 at% in the large grain layer (region II) to nearly 20 at% and 15 at% in the fine grain layer (region III), respectively. Interestingly, the content of Sn increased from around 10 at% in the large grain layer (region II) to around 15 at% in the fine grain layer (region III). Meanwhile the content of Cu and Zn decreased gradually through the whole fine grain layer and the concentration of Se decreased to around 20 at% in the fine grain layer (region III) from 25 at% in the large grain layer (region II). These results may suggest the existence of tin selenide or tin oxide compounds in the fine grain layers.

Fig. 5(d) shows the EDX line scanning through the cross section for sample D. Similarly, in region I (surface) and region II (large grain layer), the distribution for all the elements are homogeneous.

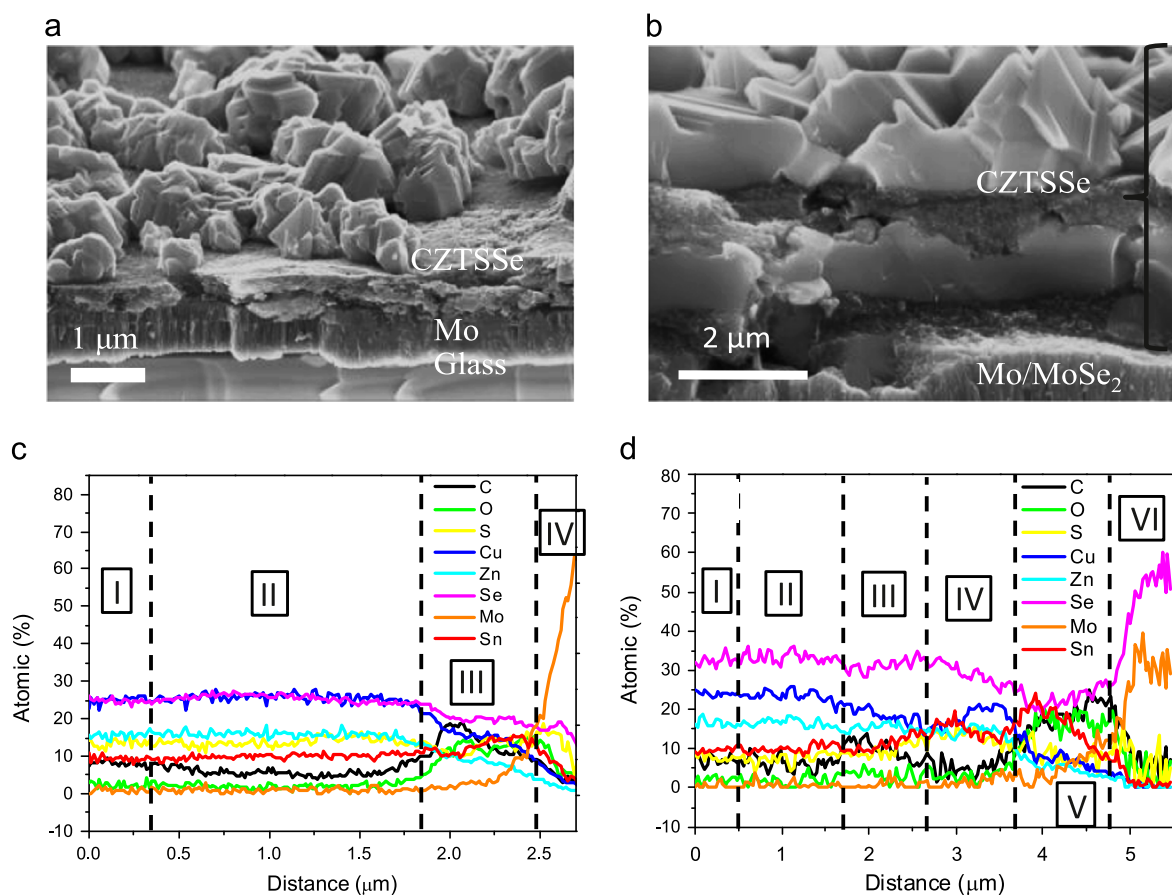


Fig. 5. Cross sectional SEM images of samples of (a) C and (b) D; EDX line scanning profile across the cross section of the samples (c) C and (d) D. In sample C, four regions were marked: region I, II, III, and IV correspond the surface of the sample, large grain layer, fine grain layer and Mo substrate. In sample D, six regions were marked across the sample: region I is the surface of the samples, regions II and IV correspond the large grain layers, and regions III and VI are the fine grain layers.

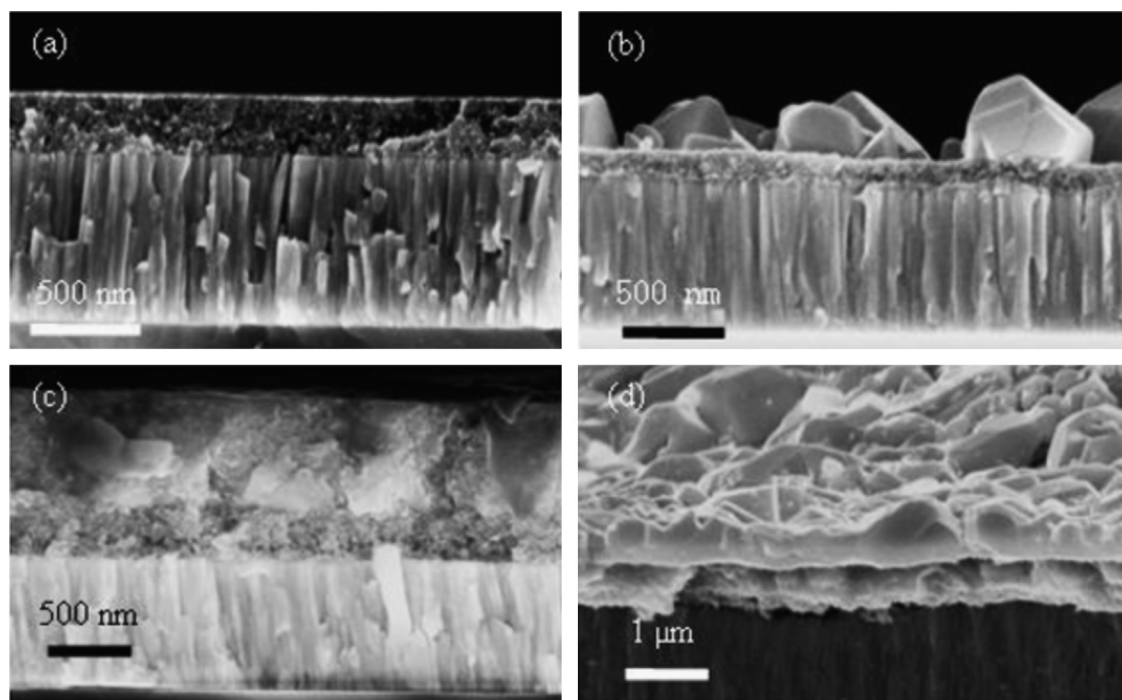


Fig. 6. Evolution of cross-sectional morphologies of samples at different stages: (a) as-deposited two layers with heat treatment 350 °C in air for 2 min, (b) two layers annealed at 580 °C in Ar/Se vapor atmosphere for 5 min, (c) two layers annealed at 580 °C in Ar/Se vapor atmosphere for 5 min plus two layers without annealing, and (d) all four layers were annealed at 580 °C in Ar/Se vapor atmosphere for 5 min.

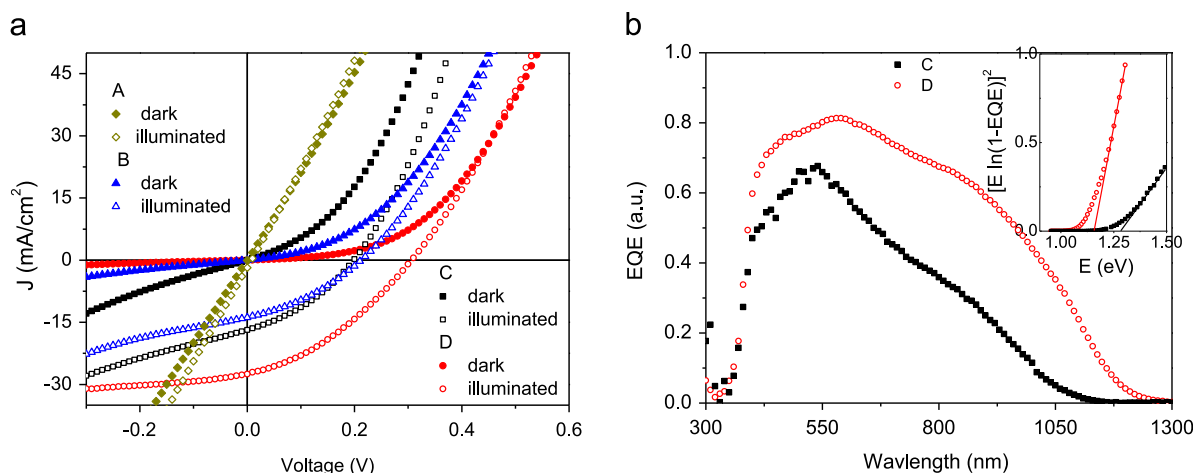


Fig. 7. (a) J - V characteristics of the best photovoltaic devices from samples A, B, C, and D under dark and simulated 1 sun AM1.5G illumination; (b) External quantum efficiency curves of the best photovoltaic cells from samples of C, and D. Inset: band gap determination from EQE data.

However, in region III (fine nanoparticle layer) the ratio of C increased by around 5 at% and the concentration of Sn increased gradually, which is accompanied by a gradual decrease of Cu. When it goes into region IV (fine grain layer near Mo), the ratio of Cu and Zn decreased significantly but both of carbon and O increased rapidly to around 20 at%. The concentration of Sn firstly increased at the interface of regions IV and V and then decreased rapidly. The surface of the Mo substrate became MoSe_2 as evidenced by around 60 at% of Se and 30 at% Mo at the surface of the substrate. The distribution of Sn, Cu and Zn is nearly homogeneous in the as-deposited C-Z-T-S precursor layers (see Fig. S5), however, both annealed samples C and D show high content of Sn and decrease of Zn and Cu near the Mo substrate. This could be due to the out diffusion of Cu and Zn during the annealing process. The highly content of carbon left in fine grain layer and the out diffusion of Cu and Zn from the fine grain layer could be the reason for the formation of layered structure.

Fig. 7(a) shows the current density–voltage (J - V) characteristic of the best devices samples A, B, C, and D under dark and simulated 1 sun AM1.5G illumination. Devices fabricated from A absorbers show nearly straight line which indicates that there is a strong shunt in the devices. As mentioned before, there are a lot of cracks in sample A, which create shunt in the devices. To reduce the cracks in the CZTSSe absorbers, the ligand-exchange layer/layers were covered with non-ligand-exchange layers/layer (samples B, and C, see detail in Table 1). Solar cells fabricated from these CZTSSe absorbers show efficiencies of 1.0% and 1.2% for samples B, and C, respectively. In addition, by using a two-step annealing process, the solar cell performance was further improved to 3.0% with open circuit voltage of 306.5 mV, short circuited current density of 27.5 mA/cm² and fill factor of 35.0%. Table 3 summarizes photovoltaic parameters for the best solar cells in samples A, B, C and D. The diode saturation current density J_{00} , dark series resistance R_S

and dark shunt resistance R_{shunt} were obtained by fitting the dark J – V curves of the corresponding devices using one diode model

$$J(V) = J_0 \left(\exp \left(\frac{q(V - R_s J(V))}{nkT} \right) - 1 \right) + \frac{V - R_s J(V)}{R_{\text{shunt}}} - J_L \quad (2)$$

where $J(V)$ is the current density, J_0 is the saturation current density, J_L is the photocurrent density, k is the Boltzmann constant, T is the temperature, n is the diode quality factor, V is the applied bias voltage, and q is the elementary electric charge, R_s is the series resistance and R_{shunt} is the shunt resistance. The best device shows the lowest diode saturation current density and the highest shunt resistance, which are also the reasons for the highest V_{OC} .

Nevertheless, this efficiency is still much lower than the record efficiencies of 12.6% reported by Wang et al. [7] who fabricated the CZTSSe solar cells from a hydrazine-based CZTSSe absorbers. One of the possible reasons for the low efficiencies is the existence of a

layered structure our CZTSSe absorbers (see Fig. 5). Another possible reason could be that the chemical composition in our CZTSSe thin film absorbers ($\text{Cu}/(\text{Zn} + \text{Sn}) = 0.72$ and $\text{Zn}/\text{Sn} = 1.0$) was not well optimized. Although it is still unclear what the optimal chemical composition is for the CZTSSe-based solar cells, the reported chemical composition of CZTSSe absorber for the high efficient CZTSSe-based solar cells is Cu-poor and Zn-rich with the metal ratio in the range of $\text{Cu}/(\text{Zn} + \text{Sn}) = 0.78$ – 0.86 , and $\text{Zn}/\text{Sn} = 1.15$ – 1.35 [28,29,32–34].

Fig. 7(b) shows the external quantum efficiency (EQE) curve of the best photovoltaic cells from samples of C, and D. The highest EQE is over 65% and 80% for devices C, and D, respectively. In addition, device of sample D shows better response than that of device from C in the infrared region, which is related to the band gap of the CZTSSe absorbers. By integration the EQE curve over the wavelength using Eq. (3), the short circuit current density were obtained to be 16.9 for devices of C, which is in good agreement with the value determined by the J – V measurement under one sun simulator. Similarly, the short circuit current density is estimated to be 28.2 mA/cm^2 from the EQE curve of device D, which is close to the value of 27.5 mA/cm^2 determined by using one sun simulator.

$$J_{\text{SC}} = \int q \text{EQE}(\lambda) \Phi_0(\lambda) d\lambda \quad (3)$$

where Φ_0 is the initial photon flux given in photons/($\text{m}^2 \text{ s}$), and q is the elementary electric charge. The band gaps of the CZTSSe absorber layers were estimated to be 1.28 eV and 1.15 eV for

Table 3
Device characteristics for the best solar cells from samples A, B, C, and D.

| Samples | Illuminated | | | | Dark | | |
|---------|-------------------------|--|--------|------------|--------------------------------------|-----------------------------------|--|
| | V_{OC} (mV) | J_{SC} (mA/cm^2) | FF (%) | η (%) | J_0 (mA/cm^2) | R_s (Ωcm^2) | R_{shunt} (Ωcm^2) |
| A | 8.1 | 0.9 | 25.0 | 0.0 | 1.46 | 2.67 | 2 |
| B | 212.4 | 13.8 | 34.2 | 1.0 | 0.36 | 2.30 | 109 |
| C | 198.6 | 16.8 | 34.9 | 1.2 | 0.61 | 1.28 | 30 |
| D | 306.5 | 27.5 | 35.0 | 3.0 | 0.22 | 2.25 | 449 |

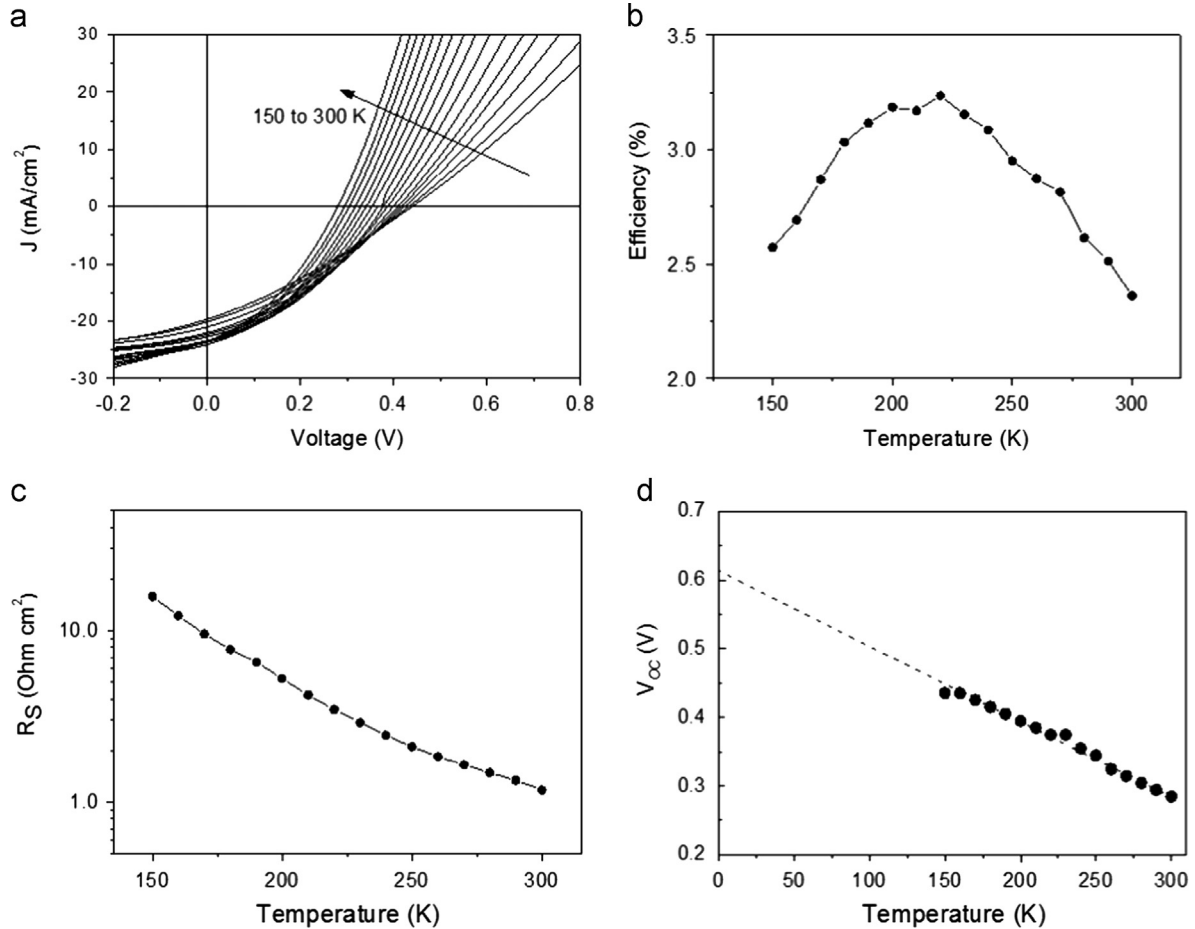


Fig. 8. (a) Temperature dependent J – V characteristics of the device from sample D. (b) Evolution of efficiencies with temperature; (c) evolution of series resistance (R_s) with temperature under dark condition. The series resistance was determined by fitting the J – V curve using the one diode model (d) open circuit voltages. The activation energy was estimated to be 0.6 eV. The measurements were performed in the temperature range of 150–300 K.

samples C and D, respectively, from the EQE data by plotting the square of $E \times \ln(1-EQE)$ versus photon energy [31]. The band gap of sample C is higher than that of sample D, which is mainly due to the higher S content in sample C than in sample D as revealed by both a larger shift of the XRD patterns in sample D towards lower angle (see Fig. 2) and a larger shift of Raman spectrum to lower wavenumber (see Fig. 3). In addition, The band gap of sample D (1.15 eV) is very close to the reported 1.13 eV for the record efficiencies solar cell [31], which means, in principle, the V_{OC} in this sample should be close to or even higher than 513.4 mV of the record solar cells [31]. However, the obtained V_{OC} 306.5 mV is far below 513.4 mV, indicating a strong recombination exists in our sample.

To identify the limitation of the device performance, temperature dependent J - V measurements were performed on the best device of sample D. Fig. 8(a) illustrates the evolution of the J - V curves as a function of temperature. The open circuit voltage of the device shifted towards higher value with decreasing temperature while the short circuit current density decreased as the temperature decreased, as shown in Fig. 8(b) and (c). The efficiencies increased drastically with decreasing temperature and saturated below 220 K after which the efficiencies collapsed. This effect can be related to the dramatic increase of series resistance in the low temperature range, as shown in Fig. 8(b). This behavior is in agreement with the literature reports for the CZTSSe-based thin films solar cells [31,35].

Fig. 8(d) shows the temperature dependent open circuit voltage for the record CZTSSe solar cells from sample D. The relationship between V_{OC} and temperature (T) is given as Eq. (4):

$$V_{OC} = \frac{E_a}{q} - \frac{AkT}{q} \ln \left(\frac{J_{00}}{J_L} \right) \quad (4)$$

where E_a , A , k , J_{00} , and J_L are the activation energy of the dominant recombination, diode ideality factor, Boltzmann constant, reverse saturation current prefactor and the photocurrent, respectively. The activation energy E_a is the intercept of the linear extrapolation of the temperature dependent V_{OC} curve when the temperature T is 0 K. The activation energy E_a was found to be 0.61 eV, which is significantly lower than the observed band gap of 1.15 eV for the current solar cell. Generally, if E_a equals to the band gap of the absorber, then the dominated recombination pathways is situated in the bulk of the absorbers; when E_a is smaller than the band gap of the absorbers, the dominated recombination is located at the interface of the heterojunction [36]. Therefore, we can conclude that in our case the dominated recombination pathway is situated at the CZTSSe and CdS interface, which is in accordance with the literature reports [30,31,37,38].

4. Conclusions

In conclusion, CZTSSe thin film absorbers were successfully prepared from the ZnS, SnS and CTS nanoparticle precursors by combination of the ligand-exchanged and non-ligand-exchanged processes. It is found that ligand-exchange with $(NH_4)_2S$ for all sequential spun coat C-Z-T-S precursors' layers resulted in cracks in the resulting CZTSSe thin films. Crack-free CZTSSe thin film absorbers can be achieved by combining the ligand-exchange and non-ligand-exchange processes. A double-layered structure with homogeneous large grain layer on top and fine grain layer near the substrate was formed when the precursor films were annealed under Se-containing atmosphere. The reasons for the formation of layered structure were found to be the existence of high content of carbon in the fine grains which serves as barrier for the growth of the nanoparticles and the highly Sn-rich in the fine grain layer which deviates from the stoichiometry of CZTSSe. No efficiency

has been observed in the devices fabricated from a CZTSSe absorber with ligand-exchange for all four sequential layers due to lots of cracks in CZTSSe thin films. By covering the ligand-exchanged layer/layers with non-ligand-exchange layers/layer, solar cells with efficiencies around 1% can be achieved. Further optimizing the deposition process of the CZTSSe thin film absorbers using a two-step annealing processes, solar cells performance was improved to 3.0%. The limitation for the device performance was found to be the high interface recombination by temperature dependent J - V analysis, which is in accordance with that of the recorded efficient CZTSSe solar cells.

Acknowledgments

This work was carried out as part of a program supported by the BMBF (Grant 03SF0363B). The authors would like to thank U. Bloeck for the TEM measurements, J. Klaer for the preparation of Mo substrates, C. Kelch and M. Kirsch for the completion of the solar cells. One of the authors (X.Z. Lin) gratefully acknowledges the financial support from the China Scholarship Council, Helmholtz Association and HZB.

Appendix A. Supporting information

Supplementary data associated with this article can be found in the online version at <http://dx.doi.org/10.1016/j.solmat.2014.08.024>.

References

- [1] M.A. Green, K. Emery, Y. Hishikawa, W. Warta, E.D. Dunlop, Solar cell efficiency tables (version 44), *Prog. Photovolt.* 22 (2014) 701–710.
- [2] B.-A. Schubert, B. Marsen, S. Cinque, T. Unold, R. Klenk, S. Schorr, H.-W. Schock, Cu_2ZnSnS_4 thin film solar cells by fast coevaporation, *Prog. Photovolt.* 19 (2011) 93–96.
- [3] I. Repins, C. Beall, N. Vora, C. DeHart, D. Kuciauskas, P. Dippo, B. To, J. Mann, W.-C. Hsu, A. Goodrich, R. Noufi, Co-evaporated $Cu_2ZnSnSe_4$ films and devices, *Sol. Energy Mater. Sol. Cells* 101 (2012) 154–159.
- [4] A. Redinger, M. Mousel, R. Djemour, L. Güttay, N. Valle, S. Siebentritt, $Cu_2ZnSnSe_4$ thin film solar cells produced via co-evaporation and annealing including a $SnSe_2$ capping layer, *Prog. Photovolt.* 22 (2014) 51–57.
- [5] A. Redinger, S. Siebentritt, Coevaporation of $Cu_2ZnSnSe_4$ thin films, *Appl. Phys. Lett.* 97 (2010) 092111.
- [6] T.K. Todorov, K.B. Reuter, D.B. Mitzi, High-efficiency solar cell with Earth-abundant liquid-processed absorber, *Adv. Mater.* 22 (2010) E156–E159.
- [7] W. Wang, M.T. Winkler, O. Gunawan, T. Gokmen, T.K. Todorov, Y. Zhu, D.B. Mitzi, Device characteristics of CZTSSe thin-film solar cells with 12.6% efficiency, *Adv. Energy Mater.* 4 (2014) (<http://dx.doi.org/10.1002/aenm.201301465>).
- [8] O. Gunawan, T.K. Todorov, D.B. Mitzi, Loss mechanisms in hydrazine-processed $Cu_2ZnSn(Se,S)_4$ solar cells, *Appl. Phys. Lett.* 97 (2010) 233506.
- [9] W. Yang, H.S. Duan, B. Bob, H. Zhou, B. Lei, C.H. Chung, S.H. Li, W.W. Hou, Y. Yang, Novel solution processing of high-efficiency Earth-abundant $Cu_2ZnSn(S,Se)_4$ solar cells, *Adv. Mater.* 24 (2012) 6323–6329.
- [10] Y. Cao, M.S. Denny Jr., J.V. Caspar, W.E. Farneth, Q. Guo, A.S. Ionkin, L.K. Johnson, M. Lu, I. Malajovich, D. Radu, H.D. Rosenfeld, K.R. Choudhury, W. Wu, High-efficiency solution-processed $Cu_2ZnSn(S,Se)_4$ thin-film solar cells prepared from binary and ternary nanoparticles, *J. Am. Chem. Soc.* 134 (2012) 15644–15647.
- [11] G.M.F. Qijie Guo, Wei-Chang Yang, Bryce C. Walker, Eric A. Stach, Hugh W. Hillhouse, Rakesh Agrawal, Fabrication of 7.2% efficient CZTSSe solar cells using CZTS nanocrystals, *J. Am. Chem. Soc.* 132 (2010) 17384–17386.
- [12] C.-J. Hsu, H.-S. Duan, W. Yang, H. Zhou, Y. Yang, Benign solutions and innovative sequential annealing processes for high performance $Cu_2ZnSn(Se, S)_4$ photovoltaics, *Adv. Energy Mater.* 4 (2014) 1301287.
- [13] W. Ki, H.W. Hillhouse, Earth-abundant element photovoltaics directly from soluble precursors with high yield using a non-toxic solvent, *Adv. Energy Mater.* 1 (2011) 732–735.
- [14] Q. Guo, G.M. Ford, W.-C. Yang, C.J. Hages, H.W. Hillhouse, R. Agrawal, Enhancing the performance of CZTSSe solar cells with Ge alloying, *Sol. Energy Mater. Sol. Cells* 105 (2012) 132–136.
- [15] Y. Sun, Y. Zhang, H. Wang, M. Xie, K. Zong, H. Zheng, Y. Shu, J. Liu, H. Yan, M. Zhu, W. Lau, Novel non-hydrazine solution processing of earth-abundant $Cu_2ZnSn(S,Se)_4$ absorbers for thin-film solar cells, *J. Mater. Chem. A* 1 (2013) 6880.
- [16] Z. Su, K. Sun, Z. Han, H. Cui, F. Liu, Y. Lai, J. Li, X. Hao, Y. Liu, M.A. Green, Fabrication of Cu_2ZnSnS_4 solar cells with 5.1% efficiency via thermal

- decomposition and reaction using a non-toxic sol–gel route, *J. Mater. Chem. A* 2 (2014) 500.
- [17] T. Schnabel, M. Löw, E. Ahlswede, Vacuum-free preparation of 7.5% efficient $\text{Cu}_2\text{ZnSn}(\text{S},\text{Se})_4$ solar cells based on metal salt precursors, *Sol. Energy Mater. Sol. Cells* 117 (2013) 324–328.
 - [18] J.J. Scragg, D.M. Berg, P.J. Dale, A 3.2% efficient kesterite device from electrodeposited stacked elemental layers, *J. Electroanal. Chem.* 646 (2010) 52–59.
 - [19] K.D.L.J. O Jeon, L.S. Oh, S.W. Seo, D.K. Lee, H. Kim, J.H. Jeong, M.J. Ko, B.S. Kim, H.J. Son, J.Y. Kim, Highly efficient copper–zinc–tin–selenide (CZTSe) solar cells by electrodeposition, *ChemSusChem* 7 (2014) 1073–1077.
 - [20] F. Jiang, S. Ikeda, T. Harada, M. Matsumura, Pure sulfide $\text{Cu}_2\text{ZnSnS}_4$ thin film solar cells fabricated by preheating an electrodeposited metallic stack, *Adv. Energy Mater.* 4 (2014) 1301381.
 - [21] A. Ennaoui, M. Lux-Steiner, A. Weber, D. Abou-Ras, I. Kötschau, H.W. Schock, R. Schurr, A. Hölzing, S. Jost, R. Hock, T. Voß, J. Schulze, A. Kirbs, $\text{Cu}_2\text{ZnSnS}_4$ thin film solar cells from electroplated precursors: novel low-cost perspective, *Thin Solid Films* 517 (2009) 2511–2514.
 - [22] X. Lin, J. Kavalakatt, K. Kornhuber, S. Levchenko, M.C. Lux-Steiner, A. Ennaoui, Structural and optical properties of $\text{Cu}_2\text{ZnSnS}_4$ thin film absorbers from ZnS and Cu_3SnS_4 nanoparticle precursors, *Thin Solid Films* 535 (2013) 10–13.
 - [23] H. Zhang, B. Hu, L. Sun, R. Hovden, F.W. Wise, D.A. Muller, R.D. Robinson, Surfactant ligand removal and rational fabrication of inorganically connected quantum dots, *Nano Lett.* 11 (2011) 5356–5361.
 - [24] X. Lin, A. Steigert, M.C. Lux-Steiner, A. Ennaoui, One-step solution-based synthesis and characterization of kuramite Cu_3SnS_4 nanocrystals, *RSC Adv.* 2 (2012) 9798.
 - [25] D.B. Mitzi, O. Gunawan, T.K. Todorov, K. Wang, S. Guha, The path towards a high-performance solution-processed kesterite solar cell, *Sol. Energy Mater. Sol. Cells* 95 (2011) 1421–1436.
 - [26] J. He, L. Sun, S. Chen, Y. Chen, P. Yang, J. Chu, Composition dependence of structure and optical properties of $\text{Cu}_2\text{ZnSn}(\text{S},\text{Se})_4$ solid solutions: an experimental study, *J. Alloys Compd.* 511 (2012) 129–132.
 - [27] L. Guo, Y. Zhu, O. Gunawan, T. Gokmen, V.R. Deline, S. Ahmed, L.T. Romankiw, H. Deligianni, Electrodeposited $\text{Cu}_2\text{ZnSnSe}_4$ thin film solar cell with 7% power conversion efficiency, *Prog. Photovoltaics* (2013), <http://dx.doi.org/10.1002/pip.2332>.
 - [28] S. Ahmed, K.B. Reuter, O. Gunawan, L. Guo, L.T. Romankiw, H. Deligianni, A high efficiency electrodeposited $\text{Cu}_2\text{ZnSnS}_4$ Solar cell, *Adv. Energy Mater.* 2 (2012) 253–259.
 - [29] Q. Guo, G.M. Ford, W.-C. Yang, B.C. Walker, E.A. Stach, H.W. Hillhouse, R. Agrawal, Fabrication of 7.2% efficient CZTSe solar cells using CZTS nanocrystals, *J. Am. Chem. Soc.* 132 (2010) 17384–17386.
 - [30] D.A.R. Barkhouse, O. Gunawan, T. Gokmen, T.K. Todorov, D.B. Mitzi, Device characteristics of a 10.1% hydrazine-processed $\text{Cu}_2\text{ZnSn}(\text{S},\text{Se})_4$ solar cell, *Prog. Photovolt.* 20 (2012) 6–11.
 - [31] T.K. Todorov, J. Tang, S. Bag, O. Gunawan, T. Gokmen, Y. Zhu, D.B. Mitzi, Beyond 11% efficiency: characteristics of state-of-the-art $\text{Cu}_2\text{ZnSn}(\text{S},\text{Se})_4$ solar cells, *Adv. Energy Mater.* 3 (2013) 34–38.
 - [32] T.K. Todorov, K.B. Reuter, D.B. Mitzi, High-efficiency solar cell with earth-abundant liquid-processed absorber, *Adv. Mater.* 22 (2010) E156–E159.
 - [33] B. Shin, O. Gunawan, Y. Zhu, N.A. Bojarczuk, S.J. Chey, S. Guha, Thin film solar cell with 8.4% power conversion efficiency using an earth-abundant $\text{Cu}_2\text{ZnSnS}_4$ absorber, *Prog. Photovolt.* 21 (2013) 72–76.
 - [34] I. Repins, C. Beall, N. Vora, C. DeHart, D. Kuciauskas, P. Dippo, B. To, J. Mann, W.-C. Hsu, A. Goodrich, R. Noufi, Co-evaporated $\text{Cu}_2\text{ZnSnSe}_4$ films and devices, *Sol. Energy Mater. Sol. Cells* 101 (2012) 154–159.
 - [35] O. Gunawan, T.K. Todorov, D.B. Mitzi, Loss mechanisms in hydrazine-processed $\text{Cu}_2\text{ZnSn}(\text{S},\text{Se})_4$ solar cells, *Appl. Phys. Lett.* 97 (2010) 233506.
 - [36] V. Nadenau, U. Rau, A. Jasenek, H.W. Schock, Electronic properties of CuGaSe_2 -based heterojunction solar cells. Part I. Transport analysis, *J. Appl. Phys.* 87 (2000) 584.
 - [37] O. Gunawan, T.K. Todorov, D.B. Mitzi, Loss mechanisms in hydrazine-processed $\text{Cu}_2\text{ZnSn}(\text{S},\text{Se})_4$ solar cells, *Appl. Phys. Lett.* 97 (2010) 233506.
 - [38] S. Tajima, H. Katagiri, K. Jimbo, N. Sugimoto, T. Fukano, Temperature dependence of $\text{Cu}_2\text{ZnSnS}_4$ photovoltaic cell properties, *Appl. Phys. Express* 5 (2012) 082302.